

Wave-equation Traveltime Tomography Unravels a Scenario of Horizontal Mantle Flow Beneath the North China Craton

Xingpeng Dong

Tsinghua University

Dinghui Yang (✉ ydh@mail.tsinghua.edu.cn)

Tsinghua University

Fenglin Niu

Rice University

Shaolin Liu

Tsinghua University

Ping Tong

Nanyang Technological University

Research Article

Keywords: North China craton (NCC), tomography , anisotropic model , Taihang Mountains

Posted Date: March 9th, 2021

DOI: <https://doi.org/10.21203/rs.3.rs-250919/v1>

License:  This work is licensed under a Creative Commons Attribution 4.0 International License.

[Read Full License](#)

Wave-equation traveltime tomography unravels a scenario of horizontal mantle flow beneath the North China craton

Xingpeng Dong¹, Dinghui Yang^{1*}, Fenglin Niu^{2,3}, Shaolin Liu^{1,4}, Ping Tong⁴

1. Department of Mathematical Sciences, Tsinghua University, Beijing 100084, China
 2. Department of Earth, Environmental and Planetary Sciences, Rice University, Houston, Texas, USA
 3. State Key Laboratory of Petroleum Resources and Prospecting, and Unconventional Petroleum Research Institute, China University of Petroleum at Beijing, Beijing, China.
 4. Division of Mathematical Sciences, School of Physical and Mathematical Sciences & Asian School of the Environment, Nanyang Technological University, Singapore

Correspondence: Dinghui Yang (E-mail: ydh@mail.tsinghua.edu.cn)

Abstract

The North China craton (NCC) was dominated by tectonic extension from late Cretaceous to Cenozoic, yet seismic studies on the relationship between crust extension and lithospheric mantle deformation are scarce. Here we present a three dimensional radially anisotropic model of NCC derived from wave-equation traveltome tomography to address this issue. We find a prominent low S-wave velocity anomaly at lithospheric mantle depths beneath the Taihang Mountains, which extends eastward with a gradually decreasing amplitude. The horizontally elongated low-velocity anomaly is also featured by a distinctive positive radial anisotropy ($V_{SH} > V_{SV}$). Combining geodetic and other seismic measurements, we speculate the presence of a horizontal mantle flow beneath central and eastern NCC, which led to the extension of the overlying crust. We suggest that the rollback of Western Pacific slab likely played a pivotal

24 role in generating the horizontal mantle flow at lithospheric depth beneath the central and
25 eastern NCC.

26 **1. Introduction**

27 The thick lithosphere with low density and water content enables cratons to float on the
28 asthenosphere and remain stable as indicated by lack of large-scale crustal deformation and
29 magmatism (Pearson, 1999). However, since the Late Mesozoic, the eastern block of NCC has
30 frequently experienced magmatic activities and multiple intense crustal deformations, which
31 suggests that the original stable craton has been modified and destroyed (Yang et al., 2008).
32 This geological phenomenon challenges the classical plate tectonics theory (e.g., McKenzie &
33 Parker, 1967; Le Pichon, 1968). Due to the coexistence of the highly extended eastern block
34 and the stable western block (Figure 1), the NCC offers a unique opportunity to address the
35 fundamental framework of the evolution of cratons (Sleep, 2004).

36 Direct evidence for a complete or partial replacement of the lithospheric mantle beneath
37 NCC comes from petrologic and geochemical studies. Geothermal studies of diamonds and
38 mantle xenoliths indicate that the thickness of the lithosphere in the eastern NCC was
39 approximately 200 km in the Paleozoic era (Griffin et al., 1992, 1998; Menzies et al., 1993).
40 Re-Os isotope dating shows that these xenoliths are remnants of Archean lithospheric mantle
41 (Gao et al., 2002; Wu et al., 2006; Zhang et al., 2008). However, geochemical studies of basalts
42 collected from the area indicate that the highly depleted Paleozoic lithosphere was somehow
43 replaced by fertile peridotites in the Cenozoic, and seismic studies suggest that the present-day
44 lithospheric thickness of the eastern NCC is approximately 80~120 km (Chen 2009; Chen et
45 al., 2009). Measurements of heat flow also show a significant increase from ~ 40 Mw/m² in the
46 Paleozoic to 80 Mw/m² in the Cenozoic (Nehru & Reddy, 1989; Rao et al., 2001; Griffin et al.,
47 2009; Karmalkar et al., 2009). The high heat flow values are close to those observed in rift
48 zones and other modern active continental areas. Previous studies suggest that the eastern NCC

49 has undergone a stage of remobilization and has experienced intense extension with lithospheric
50 root destruction (Zheng et al., 2009; Zhu et al., 2011).

51 In contrast to the consensus on the replacement of mantle lithosphere beneath the eastern
52 NCC, debates continue regarding the mechanism and dynamic processes leading to the
53 destruction of the cratonic root. At present, there are two main types of models, namely,
54 delamination (Gao et al., 2004; Wu et al., 2005; Xu et al., 2006; Deng et al., 2007) and thermal-
55 chemical erosion (Zheng et al., 2005; Menzies et al., 2007; Zhai et al., 2007), which correspond
56 to a top-down physical process and a bottom-up chemical-mechanical process, respectively. In
57 terms of delamination, several different interpretations have been proposed, such as “local
58 multiple delamination”, “lower crustal delamination” and “whole lithosphere delamination”
59 (Jull & Kelemen, 2001; Elkins-Tanton et al., 2005; Xu et al., 2002). Multiple types of erosion
60 models have also been suggested, including uniform erosion, mantle replacement and
61 peridotite-melt interactions(e.g. Zheng et al., 2005; Menzies et al., 2007; Xu, 2001). Similarly,
62 various plausible proposals have been presented for the dynamic processes that led to
63 delamination or erosion, such as continental collision between the Yangtze Craton and the NCC
64 (Montagner & Kennett, 1996), intraplate asthenospheric upwelling (Wilde et al., 2003), India-
65 Eurasia collision (Liu et al., 2004), and paleo-Pacific Plate subduction (Xu et al., 2007; Zhang
66 et al., 2009).

67 Previous models inverted from classical ray-based tomography (e.g., Tian et al., 2009;
68 Guo et al., 2014; J. Wang et al., 2014) or finite-frequency tomography (Xu et al., 2018) captured
69 stable large-scale patterns of NCC, such as the high speed and thick cratonic lithosphere of the
70 Ordos block. These models differ in detail due to significant differences in ray-tracing methods,
71 seismic phases selection and data weighting, but all models suffer from inaccurate crustal
72 correction when involving joint inversion structures of crust and upper mantle and inherent
73 theoretical limitations of approximate, asymptotic methods. Besides, complicated three
74 dimensional (3D) geological structures of NCC result in severely distorted waveforms, which
75 cannot be predicted using the imperfect one-dimensional (1D) reference model widely used in

76 traditional tomographic inversions. Wave-equation tomography completely eliminates these
77 limitations and has demonstrated significant improvements in image accuracy of the Earth's
78 interior as compared to the results obtained from traditional ray-based tomography (e.g., Tape
79 et al., 2009; Fichtner et al., 2009; Zhu et al., 2012a, 2012b; Chen et al., 2014, 2015a, 2015b;
80 Tao et al., 2018; Dong et al., 2019; Huang et al., 2020). Taking advantage of dense seismic
81 arrays deployed in NCC and wave-equation tomography techniques, we present a seismic
82 model named NCRA2020 (North China Radially Anisotropic model 2020), which reveals new
83 details of low-velocity distribution and radially anisotropic pattern that further constrain
84 lithospheric structure and infer deformation of the NCC.

85 **2. Data and Waveform tomography**

86 **2.1 Data**

87 The basement of the NCC can be divided into three first-order tectonic units: the eastern
88 NCC block, the western NCC block, and the Trans-North China Orogen in the middle, which
89 formed in the Paleoproterozoic (about 1.85 Ga) due to the collision of the eastern and western
90 blocks (Zhao et al., 2001). More specifically, the NCC consists of several subsidiary terranes,
91 such as Yinshan-Yanshan block (YYB) in the north, Ordos block (OB) in the west, Taihang
92 Mountains (THM) in the middle, North China Basin (NCB), Bohai gulf (BHG) and Tan-Lu
93 Fault Zone (TLFZ) in the East (Figure 1).

94 To obtain high-resolution 3D lithospheric images beneath the NCC, we collected
95 waveform data from 67 earthquakes, and recorded by 270 broadband stations of the permanent
96 seismic network of the China Earthquake Administration (Figure 1; Zheng et al., 2009). The
97 earthquakes have a moment magnitude of Mw4.0-6.0 that occurred within the study area. These
98 moderate size earthquakes are large enough to generate high signal-to-noise ratio (SNR)
99 waveform data at the 270 stations, yet they are still not too large to violate the point source
100 assumption employed in our inversion. Before inversion, we preprocessed these seismic data
101 by first eliminating the instrument responses from the original data and then filtering data with

102 a bandpass filter of 0.01 - 0.125 Hz. We also inverted the moment tensor of each earthquake
103 using the generalized cut-and-paste (gCAP) method (Zhu & Helmberger, 1996).

104 **2.2 Wave-equation travelttime tomography**

105 Wave-equation tomography has been developed in recent years to obtain high-resolution
106 seismic images of the Earth's interior by minimizing the misfit between predicted and observed
107 waveform data (e.g., Fichtner et al. 2009; Lailly, 1983; Liu & Tromp 2006; Tape et al., 2010).
108 An essential step in wave-equation tomography is calculating the Fréchet derivatives with
109 adjoint technique (Liu & Tromp, 2006; Tromp et al., 2005) by convoluting the forward
110 wavefield generated by seismic events and the adjoint wavefield generated by the time-reversal
111 adjoint source functions at the receivers (Tarantola et al., 1984; Tromp et al., 2005). Although
112 the adjoint method was initially applied to “full waveform inversion” in exploration seismology
113 (Gauthier et al., 1986; Mora, 1987; Tarantola et al., 1984; Pratt et al., 1998; Brossier et al., 2009;
114 Virieux & Operto, 2009), it has been combined with the finite-frequency theory for seismic
115 adjoint tomography (Marquering et al., 1998, 1999; Dahlen et al., 2000; Hung et al., 2000;
116 Montelli et al., 2004). Adjoint tomography utilizes iterative strategy to invert subsurface
117 structures based on more realistic 3D heterogeneous model and full seismic wavefield
118 simulation with highly accurate numerical methods, such as the spectral element method
119 (Komatitsch & Vilotte, 1998; Komatitsch & Tromp, 1999). Currently, local optimization based
120 on gradient descent is widely adopted to solve the wave-equation tomography problem, which
121 requires an initial model kinematically compatible with the observed data within half a
122 wavelength to prevent cycle skipping problems (Virieux & Operto, 2009). Luo and Schuster
123 (1991) attempted to extract travelttime residuals from the cross-correlation of predictions and
124 observations to construct misfit functions; this method is insensitive to cycle-skipping problems
125 and increases the probability of iterations converging to a global minimum. Therefore, we apply
126 wave-equation travelttime tomography to obtain 3D seismic velocity structure of lithosphere
127 and upper mantle beneath the NCC.

128 Our inversion involves the following three variables: compressional wave velocity (V_C),

129 vertically polarized S-wave velocity (V_{SV}) and horizontally polarized S-wave (V_{SH}) velocity.
 130 The objective function, $\delta\chi$, can be written in the form of a volume integral (Tromp et al., 2005;
 131 Fichtner et al., 2006a, 2006b) as follow:

$$132 \quad \delta\chi = \int (K_{V_c} \delta |n V_c| + K_{V_{sv}} \delta |n V_{sv}| + K_{V_{sh}} \delta |n V_{sh}|) d^3x \quad (1)$$

133 where K_{V_c} , $K_{V_{sv}}$ and $K_{V_{sh}}$ correspond to the Fréchet kernels of a compressional, SV and SH
 134 waves, respectively. We used spectral-element codes SES3D (Fichtner et al., 2009) to simulate
 135 both the forward and adjoint wavefields, and then calculated the Fréchet derivatives of (model
 136 parameters) V_C , V_{SV} and V_{SH} .

137 For the 3D complex North China lithosphere model, using full band seismic data may make
 138 inversion trapping into local minima. Therefore, we adopted a multiscale strategy and
 139 conducted the inversion in two frequency bands (8 – 50 s and 20 – 100 s) to mitigate cycle
 140 skipping. The inversion results of the low frequency band (20 - 100 s) were used as the initial
 141 velocity model of the next inversion with high frequency (8 - 50 s) data. We employed the
 142 FWEA18 (Full Waveform Inversion of East Asia in 2018; Tao et al., 2018) as our initial model.
 143 In order to minimize numerical dispersion, we paid special attention in mesh generation, i.e.,
 144 the length of each spectral element was ensured to be less than half of minimum wavelength.
 145 The open-source package FLEXWIN (Maggi et al., 2009) was used to automatically select time
 146 windows between paired synthetic and observed waveforms.

147 The overall cross-correlation travelttime misfit function $\chi(\mathbf{m})$ for the current Earth model \mathbf{m}
 148 of all the selected windows is written as

$$149 \quad \chi(\mathbf{m}) = \frac{1}{2} \frac{1}{N_\omega} \sum_{e=1}^E \sum_{i=1}^{N_\omega^s} \left[T_i^{obs} - T_i(\mathbf{m}) \right]^2 \quad (2)$$

150 where N_{ω}^s denotes the number of time windows of earthquake e , E indicates the total number
 151 of seismic events, and $N_{\omega} = \sum_{e=1}^E N_{\omega}^s$ denotes all the selected time windows. The adjoint
 152 source of the corresponding time window is calculated based on Tromp et al. (2005):

$$153 \quad f^*(t) = -[T^{obs} - T(\mathbf{m})] \frac{1}{N} \partial_t s(T - t, \mathbf{m}) \delta \mathbf{x} - \mathbf{x}_r \quad (3)$$

154 where s denotes displacement. N is a normalization factor given by

$$155 \quad N = \int_0^T s(t, \mathbf{m}) \partial_t^2 s(t, \mathbf{m}) dt \quad (4)$$

156 The gradients of all events were summed together to obtain the total gradient that suggests the
 157 direction for the model update. The gradient-based method was used for the inversion, and the
 158 model of the previous iteration was used as the initial model for the next iteration. We
 159 terminated the inversion process after 15 iterations once the reduction of the misfit residual
 160 becomes insignificant. After inversion, the mean values of traveltime shifts were significantly
 161 reduced (Figures S1).

162 **2.3 Model assessment**

163 Due to the high cost of computational resource required by wave-equation travelttime
 164 tomography, performing traditional “checkerboard” tests to assess resolution is almost
 165 unrealistic as it requires the same amount of computing as an actual structural inversion (Zhu
 166 et al., 2012b). Therefore, we used the point-spreading-function (PSF) test to assess local
 167 resolution (Fichtner & Trampert, 2011, 2012; Chen et al., 2015a). To do so, we first placed a
 168 5% low-Vsv zone at the center of the study area at a depth of 20 km (Figure S2) and computed
 169 Hessian kernels for the parameters V_C , V_{SH} , and V_{SV} (Figures S2b-2d). Although the results
 170 deviated slightly from the perturbation pattern, the main features were recovered and the
 171 tradeoffs between V_{SH} and V_{SV} (or V_C and V_{SV}) were almost negligible (Figure S2). We also
 172 conducted similar PSF resolution tests at depths of 60 and 100 km (Figures S3-S4), and the

173 results indicated that the main features of the perturbations could be recovered by our dataset.
174 To further illustrate that our model can resolve 3D variations of lithospheric mantle in specific
175 region (e.g., THM), a vertical PSF test along 39°N at depths between 85-115 km was carried
176 out and the result showed that our model is reliable (Figure S5).

177 Previous ray-based traveltimes tomographic results have revealed many characteristic
178 structures in the upper mantle beneath different geological units of the NCC (Huang & Zhao,
179 2004, 2006; Zhao et al., 2009). Compared with previous models (e.g., Tian et al., 2009),
180 NCRA2020 depicts a more continuous high-velocity variation of crystalline crust of BHG and
181 a clearer and more coherent low-velocity lithospheric mantle beneath central and eastern NCC.
182 The patterns of high and low velocity regions in NCRA2020 are roughly consistent with the
183 images of finite-frequency tomography (Xu et al., 2018). However, the amplitudes of the low
184 S-wave velocity anomalies beneath the Taihang and Yanshan mountains are much larger.

185 **3. Results and Discussions**

186 We present a series of horizontal maps of SV-wave speed to illustrate the lithospheric
187 heterogeneity beneath the NCC (Figure 2). At a depth of 20 km, the BHG shows clear high
188 shear wave velocity that further extends to the south of NCB, in contrast to eastern central
189 tectonic belt and western NCB, which are dominated by a large-scale low velocity anomaly.
190 The western part of the central tectonic belt appears to be penetrated by a high velocity anomaly
191 underlying the Ordos Basin (Figure 2a). At a depth of 60 km, both low velocity anomalies
192 expands to a greater area including the BHG. On the other hand, the high-velocity anomaly
193 beneath the OB also extends to a broader region, including a large portion of the central tectonic
194 belt (Figure 2b). Between depths of 100 and 150 km (Figure 2c-2d), the study area is dominated
195 by the widespread low velocity anomaly with a high amplitude.

196 Three vertical sections across the eastern and western parts of North China, marked as A-
197 A', B-B', and C-C' in Figure 1, further illustrate the lateral variations of lithospheric structure
198 across the NCC. In each section, the top, middle and bottom plots show, respectively, the

absolute V_{SV} of the top 60 km of the lithosphere, velocity perturbations ($\delta ln V_{SV}$) in the depth range of 40 - 200 km, and the radial anisotropy down to 200 km depth. We employed the 1-D PREM model (Dziewonski & Anderson, 1981) in computing velocity perturbations. Profile A-A' runs across the YYB, BGH and Jiaodong with significant variations in elevation (Figure 3). We defined the Moho as the isochron velocity of 4.2 km/s ($v_s^{\text{iso}} = 2v_{SH} / 3 + v_{SV} / 3$, black solid line in Figure 3A(a)). Crustal thickness decreases gradually from west to east, which is consistent with the results of receiver function studies (solid white line in Figure 3A(a), Chen 2009; Zheng et al., 2014). The shallowest Moho lies beneath the Jiaodong area, which is also featured by a strong negative radial anisotropy ($V_{SV} > V_{SH}$) (read area labeled as NA in Figure 3A(c)). This may suggest that area has experienced a unique tectonic event dominated by vertical deformation. The most prominent velocity structure shown in the perturbation map is the broad and strong low velocity anomaly beneath the central and eastern NCC (Figure 3A(b)), suggesting that the high velocity cratonic lithosphere has been replaced. In order to whether the high velocity cratonic keel was completely or partly removed, we conducted a numerical experiment. We added a thin high velocity layer that extends from 112° E to 122° E in the depth range of 45 - 85 km, and our results indicated our such a high velocity layer would be easily resolved by our inversion (Figure 4). Therefore, we concluded that the observed large depth extent of the low velocity structure is robust and the cratonic lithosphere here was completely replaced. The other two profiles (B-B' and C-C') also reveal approximately similar patterns with profile A-A' (Figures 3B and 3C).

Radial anisotropy of upper mantle may be caused by the subhorizontal lattice-preferred orientation (LPO) of olivine and its association with low-velocity zones suggests olivine alignment due to flow in the upper mantle of relatively low mechanical strength (Savage, 1999; Karato et al., 2008). Petrophysical experiments have illustrated that a small amount of melt can cause a significant decrease in seismic wave velocity. For example, Sato and Sacks (1989) found that as long as 5% of the melt in the mantle peridotite exists, it can cause the seismic wave velocity to drop by about 5%. Our model shows widespread low-velocity zones in the

226 lithospheric mantle beneath central and eastern blocks and prominent low S-wave perturbations
227 (exceed 5%) under mountains, which might indicate the presence of a certain amount of melt.
228 These weak material regions are dominated by strongly positive radial anisotropy ($V_{SH} > V_{SV}$),
229 indicating that they are subjected by intense horizontal strain, which makes them possible to
230 flow on a geological time scale. According to our model, the shear wave traveltimes in a 120
231 km thick lithosphere is about 26.7 s (the average S-wave velocity is ~4.5 km/s) associated with
232 the 4% anisotropy, then the traveltimes delay between the fast and low S-wave is ~1.1 s. The
233 average time delay of SKS wave splitting in the central-eastern part of North China is ~1.0 s
234 with the NW-SE fast S-wave direction (C.Y. Wang et al., 2014), which support our claim of
235 horizontal mantle flow. Moreover, GPS measurements show that the current crust of the North
236 China region is moving in the direction of NW-SE (Wang et al., 2001), which is also the
237 direction of subduction and retreat of the Western Pacific slab. Therefore, the reasonable
238 direction of plausible mantle flow should be NW-SE.

239 High magnesium andesites, dacites and adakites in the NCC are considered to be products
240 of the interactions between partially melted eclogites and mantle rocks (Gao et al., 2004). One
241 explanation is that crustal materials delaminated into the mantle. Based on the above
242 tomographic images, the large low-velocity regions under the Taihang and Yanshan Mountains
243 might be caused by lower crustal thickening and delamination. Due to subduction of the western
244 Pacific Plate, the crust beneath the Taihang and Yanshan Mountains thickened, which promoted
245 the transformation of the mafic lower crust into eclogites (Gao et al., 2002; Gao et al., 2004).
246 Since the eclogite is denser than the ambient mantle, it will sink into the mantle due to
247 gravitational instability (Lustrino et al., 2005; Bédard et al., 2006; Arndt & Goldstein, 1989).
248 Admittedly, crustal delamination would be much harder to occur within a craton than in an arc
249 setting, so there may be other important factors leading to lithospheric mantle instability. The
250 mantle transition zone (denotes as MTZ) is composed of wadsleyite and ringwoodite, which
251 can hold more water than the peridotite mantle, and the water content of the MTZ in eastern
252 China is at least 0.5-1 wt% (Kelbert et al., 2009). Geodynamic simulations indicate that when

253 the subducted slab interacts with the wet MTZ, the water in the MTZ will be squeezed out, and
254 part of the water entering the upper mantle would promote partial melting and form the low-
255 velocity zone (Yang & Faccenda, 2020). These molten mantle regions will promote
256 metasomatism and lead to refertilization and rejuvenation of the lithospheric mantle (Foley,
257 2008). These processes could increase the density of the lithospheric mantle and weaken it,
258 which is conducive to the process of delamination (Figure 4). Lithospheric delamination would
259 cause upwelling of magmatic materials, and these partially melted weak materials may flow
260 horizontally under long-term extension.

261 The studies of receiver function reveal that the depth of 410 km discontinuity in central
262 NCC sinks about 10 km (Xu et al., 2011), which may be caused by the temperature increase at
263 410 km discontinuity owing to the extruded water from MTZ (Yang & Faccenda, 2020). Higher
264 temperature increases the pressure required for phase transformation from α -olivine to β -
265 wadsleyite and deepen the depth of phase transformation (Bina & Helffrich, 1994). One of the
266 signs of NCC activity is extensive magmatism. During the period from 200~140 Ma, the
267 magmatic activity migrated inland from the trench, and after 140 Ma, the magmatic activity
268 migrated continuously southeastward (Zhang et al., 2014). These two stages of magmatic
269 activity represent the response of the western Pacific Plate to subduction advance and retreat,
270 respectively (Xu et al., 2018). These changes in subduction represent an external factor and the
271 dynamic background for the destruction of the NCC. The internal factor for the destruction of
272 the NCC was the exchange of material and energy between the deep and shallow levels (Zheng
273 & Dai, 2018). In addition to magmatic activity, the timing of ductile extensional metamorphic
274 core complexes in North China tends to become younger from northwest to southeast (Wang
275 et al., 2012). Magmatism and metamorphic core complexes migrated in the same direction as
276 the horizontal mantle flow mentioned above and can be interpreted as resulting from horizontal
277 mantle flow.

From the perspective of continental dynamics, there are two possible reasons for the destruction of the NCC: (1) the subduction of an oceanic plate (e.g. Xu, 2001; Zhu et al., 2011) and (2) the dynamic action of the deep mantle (e.g. Wilde et al., 2003). Simulation of the stability of the continental lithosphere shows that the thermal erosion at the bottom of typical cratonic lithospheric is limited (King et al., 2005; Hieronymus et al., 2007). Even if it is directly located above a mantle plume, a cratonic lithospheric mantle root would require more than 200 Ma to be significantly eroded. A much longer period would be required to destroy the craton. Li et al. (2016) indicated that the negative buoyancy from lithospheric thickening during orogenesis could cause delamination when the reference density of the lithospheric mantle is not lower than that of the asthenosphere. However, if the reference density of the lithospheric mantle is less than that of the asthenosphere, additional contributing factors, such as lower crust eclogitization, are required for delamination. Hu et al. (2018) suggested that significant modifications of the cratonic lithosphere in South America and Africa reflect permanent increase in lithospheric buoyancy due to plume-triggered delamination of deep lithospheric roots during the Late Cretaceous period and early Cenozoic era. Note that their conclusions are based on simulations of passive continental margin dynamics. However, the NCC has been affected by the subduction of the western Pacific Plate since the late Mesozoic, so its modification mechanism may be different. Zhu et al. (2019) suggested that the cratonic lithosphere is severely hydrated and that non-steady mantle flow develops, resulting in metasomatism, melting and weakening of the lithosphere, which ultimately leads to lithospheric thinning and cratonic destruction.

The existing observational data indicate that the subduction of the Pacific Plate under East Asia has played an important role in the destruction of the eastern NCC since the Mesozoic (Griffin et al., 1998; Wu et al., 2005; Ren et al., 2002). The subduction hanging wall of the Western Pacific lithosphere has undergone multiple stages of extension, coexisting island-arc volcanism and fore-arc extension of accretionary wedge since late Mesozoic (Zhu & Xu, 2019). A convincing explanation is that the Western Pacific plate has experienced multiple processes

of rollback. The rollback of the oceanic slab induces the upwelling magma owing to the delamination (and/or other mechanisms) to flow horizontally, resulting in continental crust extension and large-scale magmatism in the eastern NCC (Figure 5). The puzzle is that the current onset age of the Western Pacific subduction is 50 - 60 Ma (Moverly, 1972; Taylor, 1993), while the lithospheric thinning in NCC mainly occurred in the Mesozoic, probably before 110 Ma (Liu et al., 2008). Therefore, the Pacific plate lying flat in the MTZ is Cenozoic, not the source of Mesozoic lithospheric thinning in North China. A reasonable explanation is that the subduction of the western Pacific plate in Mesozoic led to the large-scale thinning of the lithosphere in North China, forming widespread low-velocity zones (LVZs) in lithospheric mantle. The dehydration of the Cenozoic western Pacific plate in the MTZ provides water (in the form of water-rich melt) for the LVZs of the lithospheric mantle (Niu, 2005, 2006), maintaining the already formed LVZs. Plate reconstruction in northeastern Asia indicates that the western Pacific oceanic plate subducted westward under East Asia along Mudanjiang-Honshu Island during the Jurassic, and that the trench retreated to the Sikhote-Alin, North Shimanto, and South Shimanto zones from ca. 137–128 Ma, ca. 130–90 Ma, and ca. 60 Ma, respectively (Liu et al., 2017). These studies provide supports for the mechanism that weak lithospheric mantle materials flowed horizontally in response to the rollback of the western Pacific slab.

323 **4. Conclusions**

324 The tectonic reanimation of the NCC indicates that the stable craton can also be modified
325 and destroyed, and this special geological phenomenon is the product of continental lithosphere
326 evolution under the subduction and rollback of the oceanic slab. A complete three-component
327 dataset including body and surface waves is inverted together with periods ranging from 8-100
328 s to obtain the 3D radially anisotropic model of NCC lithosphere. Central and eastern NCC are
329 characterized as prominent low S-wave velocity lithospheric mantle coupling with the primarily
330 horizontal stress deformation, leading support to the hypothesis of horizontal mantle flow.

331 Our model favors the subduction of the western Pacific slab during the Mesozoic as the
332 trigger for gravitationally unstable delamination. The subduction of oceanic slab makes the
333 lower crust of the central NCC thickened; besides it squeezed out the water in the MTZ,
334 resulting in partial melting and magmatism of the upper mantle. All of these make the stability
335 of lithospheric mantle decrease and eventually lose stability. The upwelling magma owing to
336 the delamination (and/or other mechanisms) was transported horizontally, and the driving force
337 of this horizontal mantle flow may stem from the rollback of the western Pacific slab (Zhu et
338 al., 2012; Liu et al., 2017). The dehydration reaction of the Cenozoic Western Pacific slab in
339 the MTZ provided sufficient water source for the maintenance of the lithospheric LVZs.

340

341 **Acknowledgements**

342 The waveform data used in this paper are available from <https://osf.io/3ukpe/>. The open
343 source software package SES3D (<http://www.cos.ethz.ch/software/production/ses3d.html>) was
344 used for numerically calculating seismic wavefields. This work was supported by the National
345 R&D Program on Monitoring, Early Warning and Prevention of Major Natural Disaster, China
346 (Grant No. 2017YFC1500301) and the Joint Earthquake Research Program of the National
347 Natural Science Foundation and the China Earthquake Administration (No. U1839206).

348

349

350 **References**

351 Arndt, N. T., Goldstein, S. L. 1989. An open boundary between lower continental crust and
352 mantle: Its role in crust formation and crustal recycling. *Tectonophysics*, 161(3-4), 201-212.
353 [https://doi.org/10.1016/0040-1951\(89\)90154-6](https://doi.org/10.1016/0040-1951(89)90154-6).

- 354 Bina, C. R., Helffrich, G. R. 1994. Phase transition Clapeyron slopes and transition zone
355 seismic discontinuity topography. *J Geophys Res*, 99, 15853-15860.
- 356 Bédard, J. H. 2006. A catalytic delamination-derived model for coupled genesis of Archaean
357 crust and sub-continental lithospheric mantle. *Geochimica et Cosmochimica Acta*, 70(5),
358 1188-1214. <https://doi.org/10.1016/j.gca.2005.11.008>.
- 359 Brossier, R., Operto, S., & Virieux, J. 2009. Seismic imaging of complex onshore structures by
360 2D elastic frequency-domain full-waveform inversion. *Geophysics*, 74, P. WCC105-
361 WCC118.
- 362 Chen, L. 2009. Lithospheric structure variations between the eastern and central North China
363 Craton from S- and P-receiver function migration. *Physics of the Earth & Planetary Interiors*,
364 173(3-4), 216-227. <https://doi.org/10.1016/j.pepi.2008.11.011>.
- 365 Chen, L., Cheng, C., & Wei, Z. G. 2009. Seismic evidence for significant lateral variations in
366 lithospheric thickness beneath the central and western North China Craton. *Earth &*
367 *Planetary Science Letters*, 286(1-2), 171-183. <https://doi.org/10.1016/j.epsl.2009.06.022>.
- 368 Chen, M., Huang, H., Yao, H., vander Hilst, R, & Niu, F. 2014. Low wave speed zones in the
369 crust beneath SE Tibet revealed by ambient noise adjoint tomography. *Geophysical Research*
370 *Letters*, 41, 334-340. doi:10.1002/2013GL058476.
- 371 Chen, M., Niu, F., Liu, Q., Tromp, J., & Zheng X. 2015a. Multiparameter adjoint tomography
372 of the crust and upper mantle beneath East Asia: 1. Model construction and comparisons.
373 *Journal of Geophysical Research: Solid Earth*, 120, 1762-1786. doi:10.1002/2014JB011638.
- 374 Chen, M., Niu, F., & Tromp J. 2015b. Mantle-driven uplift of Haigai Dome: New seismic
375 constraints from adjoint tomography. *Geophysical Research Letters*, 42, 6967-6974.
376 doi:10.1002/2015GL065018.

- 377 Chen, S., Wang, Q. S., Xu, W. M., et al. 2011. Thermal isostasy of North China and its gravity
378 isostasy and deep structure. *Chinese J. Geophys. (in chinese)*, 54(11), 2864-2875.
- 379 Dahlen, F. A., Nolet, G., & Hung, S.-H. 2000. Frechet kernels for finite-frequency traveltime -
380 I. Theory. *Geophys. J. Int.*, 141, 157-174.
- 381 Deng, J. F., Su, S. G., Niu Y. L., Liu, C., Zhao, G., Zhao, X., et al., 2007. A possible model for
382 the lithospheric thinning of North China Craton: Evidence from the Yanshanian (Jura-
383 Cretaceous) magmatism and tectonism. *Litho*, 96(1-2), 22-35.
384 <https://doi.org/10.1016/j.lithos.2006.09.009>.
- 385 Dong, X. P., Yang, D. H., Niu, F. L. 2019. Passive adjoint tomography of the crustal and upper
386 mantle beneath eastern Tibet with a W2-norm misfit function. *Geophysical Research Letters*,
387 46, 12986–12995.
- 388 Elkins-Tanton L. T. 2005. Continental magmatism caused by lithospheric delamination. In:
389 Foulger G R, Natland J H, Presnall S C, et al, eds. Plates, Plumes, and Paradigms. Geol Soc
390 Am Spec Pap, 388, 449-462.
- 391 Fichtner, A., Bunge, H.-P., Igel, H. 2006a. The adjoint method in seismology - I. Theory.
392 *Physics of the Earth and Planetary Interiors* 157, 86-104.
- 393 Fichtner, A., Bunge, H.-P., Igel, H. 2006b. The adjoint method in seismology - II. Applications:
394 traveltimes and sensitivity functionals. *Physics of the Earth and Planetary Interiors* 157,
395 105-123.
- 396 Fichtner, A., Kennett, B. L. N., Igel, H., & Bunge H. P. 2009. Full seismic waveform
397 tomography for upper-mantle structure in the Australasian region using adjoint methods.
398 *Geophysical Journal International*, 179 (3), 1703-1725. <https://doi.org/10.1111/j.1365-246X.2009.04368.x>.

- 400 Fichtner, A., & Trampert, J. 2011. Hessian kernels of seismic data functionals base upon adjoint
401 techniques. *Geophysical Journal International*, 185, 775-798.
- 402 Fichtner, A., & Trampert, J. 2012. Resolution analysis in full waveform inversion. *Geophysical*
403 *Journal International*, 187, 1604-1624.
- 404 Foley, S. F. 2008. Rejuvenation and erosion of the cratonic lithosphere. *Nature Geoscience*, 1:
405 503-510 .
- 406 Gao, S., Rudnick, R. L., Carlson, R. W., McDonough, W. F., & Liu Y. S. 2002. Re-Os evidence
407 for replacement of ancient mantle lithosphere beneath the North China Craton. *Earth &*
408 *Planetary Science Letters*, 198 (3-4), 307-322. [https://doi.org/10.1016/S0012-821X\(02\)00489-2](https://doi.org/10.1016/S0012-821X(02)00489-2).
- 410 Gao, S., Rudnick, R. L., Yuan, H. L., Liu, X. M., Liu, Y. S., Xu, W. L., et al. 2004. Recycling
411 lower continental crust in North China Craton. *Nature*, 432, 892-897.
- 412 Gauthier, O., Virieux, J., & Tarantola, A. 1986. Two-dimensional nonlinear inversion of
413 seismic waveforms: numerical results. *Geophysics*, 51, 1387-1403.
- 414 Griffin, W.L., O' Reilly, S.Y., Ryan, C.G. 1992. Composition and thermal structure of the
415 lithosphere beneath South Africa, Siberia and China: porton microprobe studies. Abstract of
416 the International Symposium on Cenozoic Volcanic Rocks and Deep-seated Xenoliths of
417 China and its Environs. Beijing, 65-66.
- 418 Griffin, W.L., Zhang, A.D., O' Reilly, S.Y., Ryan, C.G. 1998. Phanerozoic evolution of the
419 lithosphere beneath the Sino-Korean craton. In Mantle Dynamics and Plate Interactions in
420 East Asia (eds. Flower MFJ, Chung SL, Lo CH, Lee TY). Am. Geophy. Union, Washington,
421 D. C., Geodyn. Ser., 27, 107-126.

- 422 Guo, H L, Xu, P F, Zhang, F Q. 2014. P wave velocity structure of the North China Craton and
423 West Pacific active continental margin: exploration for dynamic processes of lithospheric
424 thinning. *Chinese J. Geophys. (in Chinese)*, 57(7), 2352-2361. Doi: 10.6038/cjg20140729.
- 425 Hieronymus, C. F., Shomali, Z. H., Pedersen, L. B. A. 2007. Dynamical model for generating
426 sharp seismic velocity contrasts underneath continents: Application to the Sorgenfrei-
427 Tornquist Zone. *Earth & Planetary Science Letters*, 262(1-2), 77-91.
428 <https://doi.org/10.1016/j.epsl.2007.07.043>.
- 429 Hu J, Liu L, Faccenda M, et al. 2018. Modification of the Western Gondwana craton by plume–
430 lithosphere interaction. *Nature Geoscience*, 11(3), 203-210.
- 431 Huang, J., Zhao, D. 2004. Crustal heterogeneity and seismotectonics of the region around
432 Beijing, China. *Tectonophysics*, 385, 159-180.
- 433 Huang, J., Zhao, D. 2006. High-resolution mantle tomography of China and surrounding
434 regions. *J Geophys Res*, 111: B09305.
- 435 Huang, X., Yang, D., Tong, P., Gao, Y., Shi, Y., Wu, H. 2020. Quasi-waveform seismic
436 tomography of crustal structures in the capital circle region of China, *Science China-Earth
437 Sciences*, DOI: 10.1007/s11430-019-9663-4.
- 438 Hung, S.-H., Dahlen, F. A., & Nolet, G. 2000. Frechet kernels for finite-frequency traveltimes -
439 II. Examples. *Geophys. J. Int.*, 141, 175-203.
- 440 Jull, m., Kelemen, P. B. 2001. On the conditions for lower crustal convective instability. *J
441 Geophys Res*, 106, 6423-6446.
- 442 Karato, S., Jung, H., Katayama, I., et al. 2008. Geodynamic significance of seismic anisotropy
443 of the upper mantle: New insights from laboratory studies. *Annual Review of Earth and
444 Planetary Sciences*, 36, 59-95.

- 445 Karmalkar, N. R., Duraiswami, R. A., Chalapathi Rao, N. V. 2009. Mantle-derived mafic-
446 ultramafic xenoliths and the nature of Indian sub-continental Lithosphere. *Journal of the*
447 *Geological Society of India*, 73, 657-679. <https://doi.org/10.1007/s12594-009-0051-7>.
- 448 Kelbert, A., Schultz, A. & Egbert, G. 2009. Global electromagnetic induction constraints on
449 transition-zone water content variations. *Nature*, 460, 1003–100.
- 450 King, S. D. 2005. Archean cratons and mantle dynamics. *Earth & Planetary Science Letters*,
451 234(1-2), 1-14. <https://doi.org/10.1016/j.epsl.2005.03.007>.
- 452 Komatitsch, D., & Villette, J. 1998. The spectral element method: an efficient tool to simulate
453 the seismic response of 2D and 3D geological structures. *Bulletin of the Seismological*
454 *Society of America*, 88, 368-392.
- 455 Komatitsch, D., & Tromp, J. 1999. Introduction to the spectral-element method for 3-D seismic
456 wave propagation. *Geophys. J. Int.*, 139, 806-822.
- 457 Lailly, P. 1983. The seismic inverse problem as a sequence of before stack migrations. In
458 conference on inverse scattering theory and application, Society for industrial and applied
459 mathematics, 206-220.
- 460 Le Pichon, X. 1968. Sea-floor spreading and continental drift, *J. Geophys. Res.* B73, 3661-
461 3697.
- 462 Li, Z. H., Liu, M. and Gerya, T. 2016. Lithosphere delamination in continental collisional
463 orogens: A systematic numerical study, *J. Geophys. Res. Solid Earth*, 121,
464 doi:10.1002/2016JB013106.
- 465 Liu, M., Cui, X., Liu, F. 2004. Cenozoic rifting and volcanism in eastern China: A mantle
466 dynamic link to the Indo-Asian collision? *Tectonophysics*, 393(1-4), 29-42.
467 <https://doi.org/10.1016/j.tecto.2004.07.029>.

- 468 Liu, Q. & Tromp, J. 2006. Finite-frequency kernels based on adjoint methods, *Bull. Seism. Soc.*
469 *Am.*, 96, 2283-2297.
- 470 Liu, S. F., Michael, G., Ma, P. F., Zhang, B. 2017. Reconstruction of northeast Asian
471 deformation integrated with western Pacific plate subduction since 200 Ma. *Earth-Sci*
472 *Rev*, 175, 114–142.
- 473 Liu, Y., Gao, S., Kelemen, P. B., Xu, W. 2008. Recycled crust controls contrasting source
474 compositions of Mesozoic and Cenozoic basalts in the North China Craton. *Geochimica et*
475 *Cosmochimica Acta*, 72(9), 2349-2376.
- 476 Lustrino, M. 2005. How the delamination and detachment of lower crust can influence basaltic
477 magmatism. *Earth-Science Reviews*, 72(1-2), 21-38.
478 <https://doi.org/10.1016/j.earscirev.2005.03.004>.
- 479 Luo, Y., Schuster, G. T. 1991. Wave-equation traveltimes inversion. *Geophysics*, 56, 645-653.
- 480 McKenzie, D P, Parker, R L. 1967. The North Pacific, an example of tectonics on a sphere,
481 *Nature*, 216, 1276–1280.
- 482 Maggi, A., Tape, C., Chen, M., Chao, D., & Tromp, J. 2009. An automated time-window
483 selection algorithm for seismic tomography. *Geophysical Journal International*, 178(1),
484 257-281. <https://doi.org/10.1111/j.1365-246X.2009.04099.x>.
- 485 Marquering, H., Nolet, G., & Dahlen, F 1998. Three-dimensional waveform sensitivity kernels.
486 *Geophys. J. Int.*, 132, 521-534.
- 487 Marquering, H., Dahlen, F , & Nolet, G. 1999. Three-dimensional sensitivity kernels for finite-
488 frequency traveltimes: the banana-doughnut paradox. *Geophys. J. Int.*, 137, 805-815.
- 489 Montelli, R., Nolet, G., Dahlen, F., Masters, G., Engdahl, E., & Hung, S. 2004. Finite-
490 Frequency Tomography Reveals a variety of Plumes in the Mantle. *Science*, 303, 338-343.

- 491 Menzies, M. A., Fan, W. M., Zhang, M. 1993. Palaeozoic and Cenozoic lithoprobe and the loss
492 of > 120 km of Archean lithosphere, Sino-Korean craton, China. In Magmatic Processes and
493 Plate Tectonic (eds. Prichard HM, Alabaster T, Harris NBW, Neary CR). *Geological Society*,
494 76(1), 71-81.
- 495 Menzies, M. A., Xu, Y. G., Zhang, H. F., Fan W. M. 2007. Integration of geology, geophysics
496 and geochemistry: A key to understanding the North China Craton. *Lithos*, 96(1-2), 1-21.
497 <https://doi.org/10.1016/j.lithos.2006.09.008>.
- 498 Moberly, R. 1972. Origin of lithosphere behind island arcs with reference to the western Pacific.
499 *Geological Society of American Memoir*, 132, 35-55.
- 500 Montagner J. P., Kennett, B. L. N. 1996. How to reconcile body-wave and normal-mode
501 reference Earth models? *Geophysical Journal International*, 125, 229-248,
502 doi:10.17611/DP/10131347.
- 503 Mora, P. 1987. Nonlinear two-dimensional elastic inversion of multioffset seismic data.
504 *Geophysics*, 52, 1211-1228.
- 505 Nehru, C. E., Reddy, A. K. 1989. Ultramafic xenoliths from Wajrakarur kimberlites, India. In:
506 Ross J, Jacques A L, Ferguson K, et al., eds. Kimberlites and Related Rocks, Proceedings of
507 the Fourth International Kimberlite Conference. Vol. 2. Geol Soc Australia Special Publ, 14,
508 745-759.
- 509 Niu, Y. L. 2005. On the great mantle plume debate. *Chinese Science Bulletin*, 50, 1537-1540.
- 510 Niu, Y. L. 2006. Continental lithospheric thinning results from hydration weakening, not
511 “delaminationn”, and is a special consequence of plate tectonics, for “mantleplume.org”.
512 <http://www.mantleplumes.org/Hydration.html>.
- 513 Pearson, D. G. 1999. The age of continental roots. *Lithos*, 48, 171–194.

- 514 Pratt, R., Shin, C., & Hicks, G. J. 1998. Gauss-Newton and full Newton methods in frequency-
515 space seismic waveform inversion. *Geophysical Journal International*, 133, 341-362.
- 516 Rao, K. R. P., Rao K. N., Dhakate M. V., et al. 2001. Petrology and mineralogy of mantle
517 xenoliths of Wajrakarur and Narayanpet kimberlite fields, Andhra Pradesh, India. *Geol
518 Survey India Special Publ*, 58, 577-591.
- 519 Ren, J. Y., Tamaki, K., Li, S. T., et al. 2002. Late Mesozoic and Cenozoic rifting and its
520 dynamic setting in Eastern China and adjacement areas. *Tectonophysics*, 344, 175-205.
- 521 Savage, M. K. 1999. Seismic anisotropy and mantle deformation: what have we learned from
522 shear wave splitting. *Reviews of Geophysics*, 37(1), 65-106.
- 523 Sato, H, Sacks, I. S. 1989. The use of laboratory velocity data for estimating temperature and
524 partial melt fraction in the low velocity zone. *J Geophys Res*, 94, 5689–5704.
- 525 Sleep, N.H. 2004. Evolution of the continental lithosphere. *Annu Rev Earth Planet Sci*, 33 (1),
526 369-393.Doi: 10.1146/annurev.earth.33.092203.122643.
- 527 Tape, C., Liu, Q., Maggi, A., & Tromp J. 2009. Adjoint tomography of the southern California
528 crust, *Science*, 325, 988-992. Doi: 10.1126/science.1175298.
- 529 Tape, C., Liu Q., Maggi, A. & Tromp, J. 2010. Seismic tomography of the southern California
530 crust based on spectral-element and adjoint methods. *Geophysical Journal International*, 180,
531 433-462.
- 532 Tao, K., Grand, S. P., Niu, F. 2018. Seismic structure of the upper mantle beneath eastern Asia
533 from full waveform seismic tomography. *Geochemistry, Geophysics, Geosystems*, 19, 2732-
534 2763. <https://doi.org/10.1029/2018GC007460>.
- 535 Taylor, B. 1993. Island arcs, deep sea trenches, and back-arc basins. *Oceanus*, 35, 17-25.

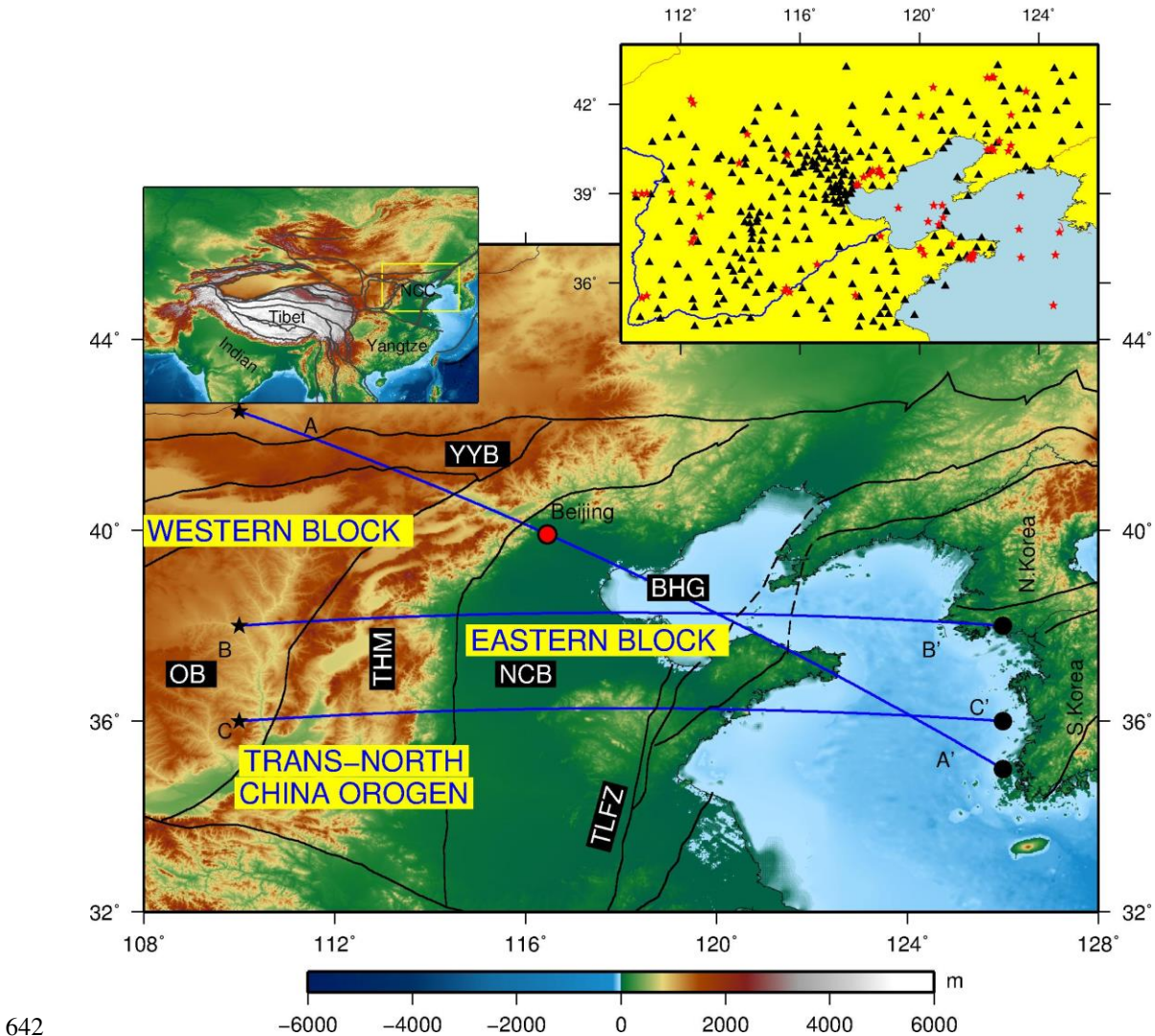
- 536 Tarantola, A. 1994. Inversion of seismic reflection data in the acoustic approximation.
- 537 *Geophysics*, 49, 1259-1266.
- 538 Tian, Y., Zhao, D., Sun, R., Teng J. W. 2009. Seismic imaging of the crust and upper mantle
539 beneath the North China Craton. *Physics of the Earth & Planetary Interiors*, 172(3), 169-
540 182. <https://doi.org/10.1016/j.pepi.2008.09.002>.
- 541 Tromp, J., Tape, C., & Liu, Q. Y. 2005. Seismic tomography, adjoint methods, time reversal
542 and banana-doughnut kernels. *Geophysical Journal International*, 160(1), 195-216.
543 <https://doi.org/10.1111/j.1365-246X.2004.02453.x>.
- 544 Virieux, J., & Operto, S. 2009. An overview of full-waveform inversion in exploration
545 geophysics. *Geophysics*, 74, WCC1-WCC26.
- 546 Wang, C. Y, Chang, L. J., Ding, Z. F., et al. 2014. Upper mantle anisotropy and crust-mantle
547 deformation pattern beneath the Chinese mainland. *Science China: Earth Sciences*, 57, 132-
548 143.
- 549 Wang, J., H. Wu, and D, Zhao. 2014. P wave radial anisotropy tomography of the upper mantle
550 beneath the North China Craton, *Geochem. Geophys. Geosyst.*, 15, 2195-2210.
- 551 Wang, Q., Zhang, P. Z., Freymueller, J., Bilham, R., Larson K., Lai, X., et al. 2001. Present-
552 day crustal deformation in China constrained by global positioning system measurements.
553 *Science*, 294, 574-577. Doi: 10.1126/science.1063647.
- 554 Wang, T., Guo, L., Zheng, Y. D., Donskaya, T., Gladkochub, S., Zeng, L. S., Li, J. B., Wang,
555 Y. B., Mazukabzov, A. 2012. Timing and processes of late Mesozoic mid-lower-crustal
556 extension in continental NE Asia and implications for the tectonic setting of the destruction
557 of the North China Craton: Mainly constrained by zircon U-Pb ages from metamorphic core
558 complexes, *Lithos*, 154, 315-345.

- 559 Wilde, S. A., Zhou, X., Nemchin, A. A., Sun, M. 2003. Mesozoic crust-mantle interaction
560 beneath the North China Craton: A consequence of the dispersal of Gondwanaland and
561 accretion of Asia. *Geology*, 31(9), 817-820. Doi: 10.1130/G19489.1.
- 562 Wu, F. Y., Lin, J. Q., Wilde S. A., Zhang, X., Yang, J. 2005. Nature and significance of the
563 Early Cretaceous giant igneous event in eastern China. *Earth & Planetary Science Letters*,
564 233, 103-119. <https://doi.org/10.1016/j.epsl.2005.02.019>.
- 565 Wu, F. Y., Walker, R. J. Yang, Y. H., Yuan, H. L., & Yang, J. H. 2006. The chemical-temporal
566 evolution of lithospheric mantle underlying the North China Craton. *Geochim. Cosmochim.
567 Acta*, 70(19), 5013-5034. <https://doi.org/10.1016/j.gca.2006.07.014>.
- 568 Xu, Y. G. 2001. Thermo-tectonic destruction of the Archean lithospheric keel beneath the Sino-
569 Korean Craton in China: Evidence, timing and mechanism. *Phys Chem Earth*, 26, 747-757.
- 570 Xu, J. F., Shinjo, R., Defant, M. J., Wang, Q., and Rapp, R. P. 2002. Origin of Mesozoic adakitic
571 intrusive rocks in the Ningzhen area of east China: Partial melting of delaminated lower
572 continental crust? *Geology*, 30, 1111-1114.
- 573 Xu, W. L., Gao, S., Wang, Q. H., Liu, Y. S. 2006. Mesozoic crustal thickening of the eastern
574 North China Craton: Evidence from eclogite xenoliths and petrologic implications. *Geology*,
575 34(9), 721-724. Doi: 10.1130/G22551.1.
- 576 Xu, W. W., Zheng, T. Y., Zhao, L. 2011. Mantle dynamics of the reactivating North China
577 Craton: Constraints from the topographies of the 410-km and 660-km discontinuities. *Sci
578 China Earth Sci*, 54, 881–887.
- 579 Xu, X B., Zhao, L., Wang, K., Yang, J F. 2018. Indication from finite-frequency tomography
580 beneath the North China Craton: The heterogeneity of craton destruction. *Science China
581 Earth Sciences*, 61(9), 1238-1260. <https://doi.org/10.1007/s11430-017-9201-y>.

- 582 Xu, Y. G. 2007. Diachronous lithospheric thinning of the North China Craton and formation of
583 the Daxin'anling-Taihangshan gravity lineament. *Lithos*, 96(1), 281-298.
584 <https://doi.org/10.1016/j.lithos.2006.09.013>.
- 585 Xu, Y. G., Li, H. Y., Hong, L. B., Ma, L., Ma, Q., Sun, M. D. 2018. Generation of Cenozoic
586 intraplate basalts in the big mantle wedge under eastern Asia. *Science China Earth Sciences*,
587 61(7), 869–886. <https://doi.org/10.1007/s11430-017-9192-y>.
- 588 Yang, J. H., Wu, F. Y., Wilde, S. A., et al. 2008. Mesozoic decratonization of the North China
589 Block. *Geology*, 36, 467–470.
- 590 Zhang, H. F., Goldstein, S., Zhou, X. H., Sun, M., Zheng, J. P., & Cai Y. 2008. Evolution of
591 subcontinental lithospheric mantle beneath eastern China: Re – Os isotopic evidence from
592 mantle xenoliths in Paleozoic kimberlites and Mesozoic basalts. *Contrib. Mineral. Petrol.*,
593 155(3), 271-293. <https://doi.org/10.1007/s00410-007-0241-5>.
- 594 Zhang, J. J., Zheng, Y. F., Zhao, Z. F. 2009. Geochemical evidence for interaction between
595 oceanic crust and lithospheric mantle in the origin of Cenozoic continental basalts in east-
596 central China. *Lithos*, 110, 305-326. <https://doi.org/10.1016/j.lithos.2009.01.006>.
- 597 Zhang, S H., Zhao, Y., Davis, G. A., Ye, H., Wu, F. 2014. Temporal and spatial variations of
598 Mesozoic magmatism and deformation in the North China Craton: Implications for
599 lithosphere thinning and decratonization. *Earth-Sci Rev*, 131(4), 49-87.
600 <https://doi.org/10.1016/j.earscirev.2013.12.004>.
- 601 Zhai, M. G., Fan, Q. C., Zhang, H. F., Sui, J., Shao, J. 2007. Lower crustal processes leading to
602 Mesozoic lithospheric thinning beneath eastern North China: Underplating, replacement and
603 delamination. *Lithos*. 96(1-2), 36-54. <https://doi.org/10.1016/j.lithos.2006.09.016>.

- 604 Zhao, G. C., Wilde, S. A., Cawood, P. A., Sun, M., Lu, L. Z. 2001. Archean blocks and their
605 boundaries in the North China Craton: lithological, geochemical, structural and P-T path
606 constraints and tectonic evolution. *Precambrian Research*, 107, 45-73.
- 607 Zhao, L., Allen, R. M., Zheng T., Huang, S. H. 2009. Reactivation of Archean craton:
608 constraints from P- and S-wave tomography in North China. *Geophysical Research Letters*,
609 36, L17306. <https://doi.org/10.1029/2009GL039781>.
- 610 Zheng J. P., Griffin W. L., O'Reilly S. Y., Liou, J. G., Zhang, R. Y., Lu, F. 2005. Late
611 Mesozoic-Eocene mantle replacement beneath the eastern North China Craton: Evidence
612 from the Paleozoic and Cenozoic peridotite xenoliths. *Inter Geol Rev*, 47(5), 457-472.
613 <https://doi.org/10.2747/0020-6814.47.5.457>.
- 614 Zheng, J. P. 2009. Comparison of mantle-derived materials from different spatiotemporal
615 settings: Implications for destructive and accretional processes of the North China Craton.
616 *Chinese Sci Bull*, 54 (14), 1990-2007. <https://doi.org/10.1007/s11434-009-0308-y>.
- 617 Zheng, J. P., Dai, H. K. 2018 . Subduction and retreating of the western Pacific plate resulted
618 in lithospheric mantle replacement and coupled basinmountain respond in the North China
619 Craton. *Science China Earth Sciences*, 61(4), 406–424. <https://doi.org/10.1007/s11430-017-9166-8>.
- 621 Zheng, X., Ouyang, B., Zhang, D., Yao, Z., Liang, J., & Zheng, J. 2009. Technical system
622 construction of Data Backup Center for China Seismograph Network and the data support to
623 researches on the Wenchuan earthquake (in chinese). *Chinese J. Geophys. (in chinese)*, 52(5),
624 1412-1417.
- 625 Zhu, H., Bozdağ, E., Peter, D., & Tromp, J. 2012a. Seismic wavespeed images across the
626 Iapetus and Tornquist suture zones. *Geophysical Research Letters*, 39, L18304,
627 doi:10.1029/2012GL053053.

- 628 Zhu, H., Bozdağ, E., Peter, D., & Tromp, J. 2012b. Structure of the European upper mantle
629 revealed by adjoint tomography. *Nat. Geosci.*, 5(7), 493-498.
630 <https://doi.org/10.1038/ngeo1501>.
- 631 Zhu, H., Bozdağ, E., Duffy, T. S., & Tromp, J. 2013. Seismic attenuation beneath Europe and
632 the North Atlantic: Implications for water in the mantle. *Earth & Planetary Science Letters*,
633 381(4), 1-11. <https://doi.org/10.1016/j.epsl.2013.08.030>.
- 634 Zhu, L., Helmberger, D.V. 1996. Advancement in source estimation techniques using
635 broadband regional seismograms. *Bull. Seism. Soc. Am.*, 86 (5), 1634-1641.
- 636 Zhu, R. X., Chen, L., Wu, F. Y., Liu, J. L. 2011. Timing, scale and mechanism of the destruction
637 of the North China Craton. *Sci China Earth Sci*, 54, 789-797. <https://doi.org/10.1007/s11430-011-4203-4>.
- 639 Zhu, R., Xu, Y. 2019. The subduction of the west Pacific plate and the destruction of the North
640 China Craton. *Science China Earth Sciences*, 62, 1340–1350.



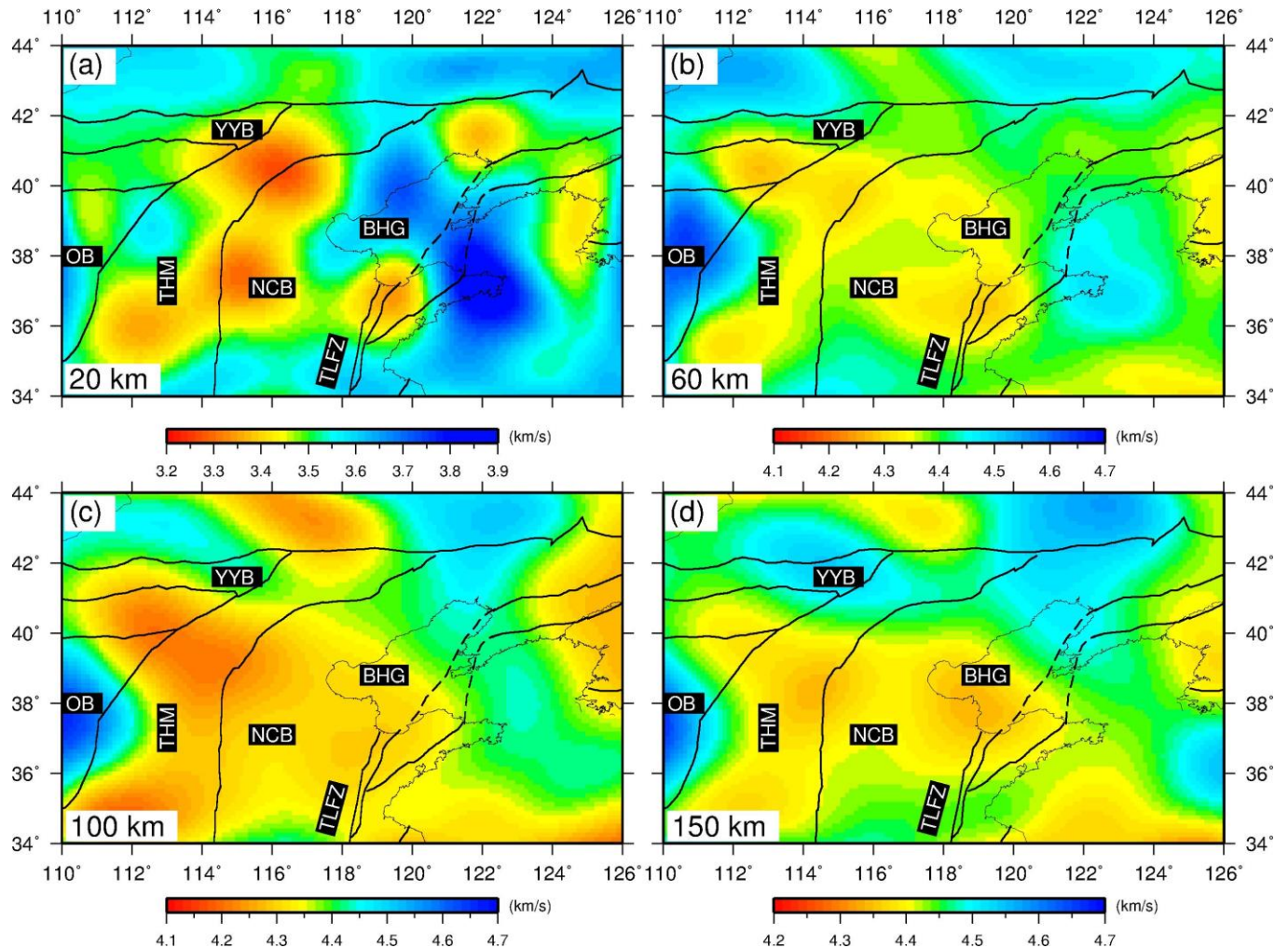
642 **Figure 1. Geological and topographic map of the North China Craton.** Blue lines A-A', B-
643 B' and C-C' indicate the location of three vertical profiles. YYB: Yinshan-Yanshan Block; OB:
644 Ordos Block; THM: Taihang Mountains; NCB: North China Basin; BHG: Bohai Gulf; TLFZ:
645 Tan-Lu Fault Zone. The left inset shows the location of NCC in East Asia; the right inset shows
646 the distribution of earthquakes (red stars) and seismic stations (black triangles) in the study.
647

648

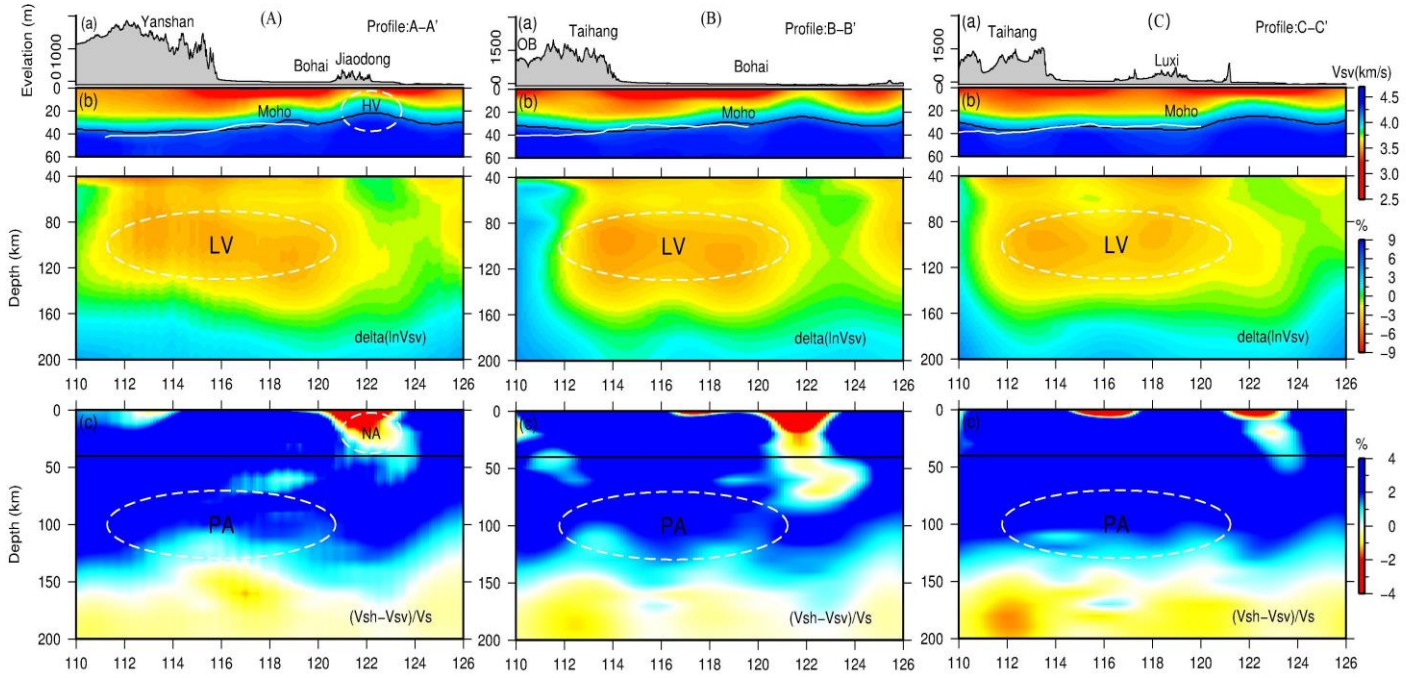
649

650

651

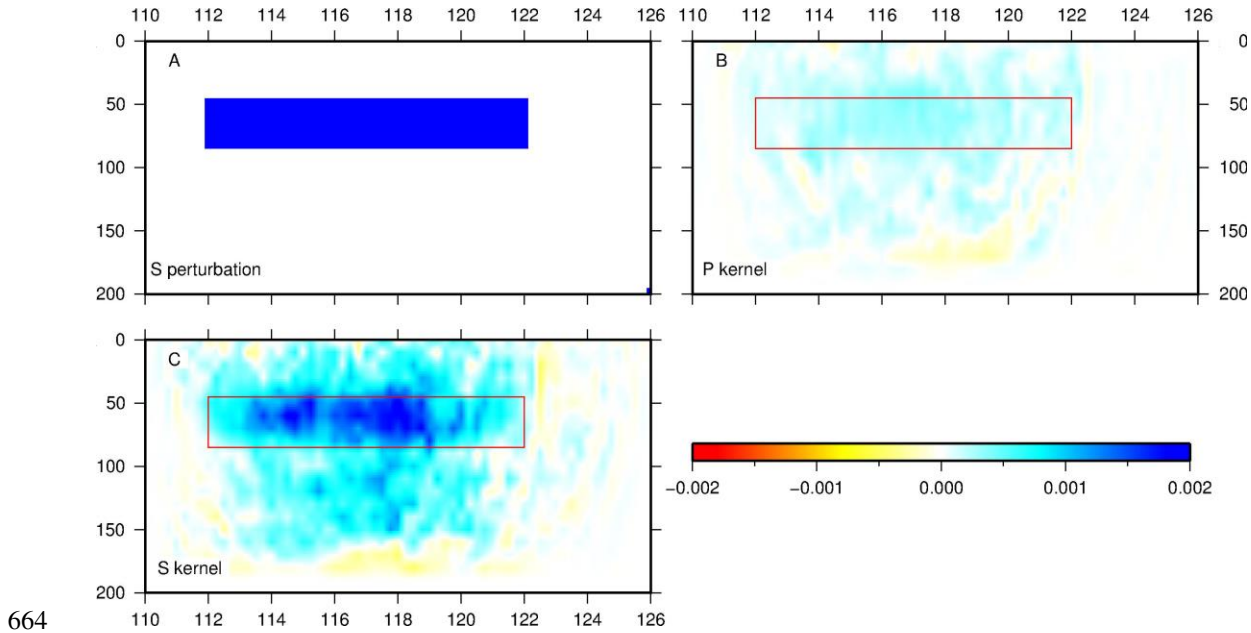
652 **Figure 2. Map views of Sv-wave velocity at four depths. (a) 20 km, (b)**

653 and (c) 100 km.

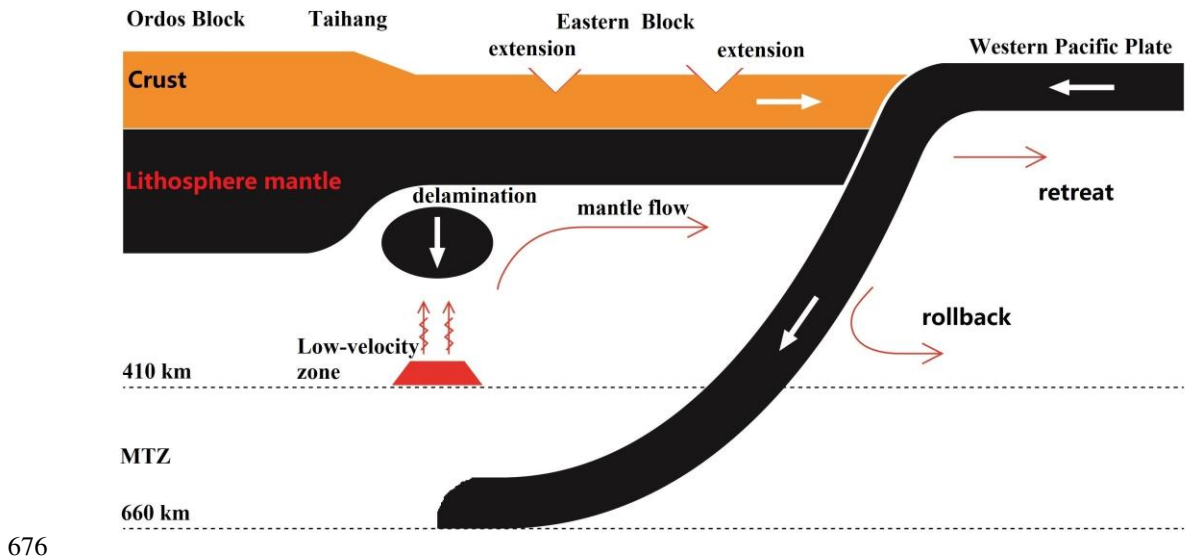


654

655 **Figure 3. Three vertical cross sections with surface elevation, velocity anomaly and radial**
 656 **anisotropy along profile A-A' (A), B-B' (B) and C-C' (C).** Surface altitude (top, a), Sv-wave
 657 velocity anomalies (middle, b), and radial anisotropy $(V_{sh}-V_{sv})/V_s$ (bottom, c). For sub-graph
 658 b, absolute velocity is adopted for the crust (top 60 km), and velocity perturbation is adopted in
 659 upper mantle (40-200 km) with reference model: PREM (Dziewonski & Anderson, 1981).
 660 White solid line denotes the depth of Moho obtained from receiver function (Chen 2009; Zheng
 661 et al., 2014); black solid line denotes the depth of Moho derived from reference shear wave
 662 velocity of 4.2 km/s. LV: low velocity; HV: high velocity; NA: negative anisotropy; PA:
 663 positive anisotropy.



664 **Figure 4. Sensitivity test of Shear wave in the lower crust along 37° N between the depth
665 of 45 km and 85 km.** (a) input high Shear velocity perturbation, (b) sensitivity kernel of P
666 wave, (c) sensitivity kernel of S wave. The unit of the color bar is $1 \times 10^{-10} \text{ s}^2 \text{m}^{-4}$.
667
668
669
670
671
672
673
674
675



677 **Figure 5. The subduction, rollback and retreat of the western Pacific Plate cause the**
 678 **delamination, horizontal mantle flow and continental crust extension of the NCC. The red**
 679 **trapezoidal area represents the low-velocity zone formed by the subducting slabs squeezing out**
 680 **the water in the mantle transition zone (denotes as MTZ); the water enters the upper mantle and**
 681 **causes partial melting. The black ellipse indicates the delamination of lithosphere due to gravity**
 682 **instability.**

Figures

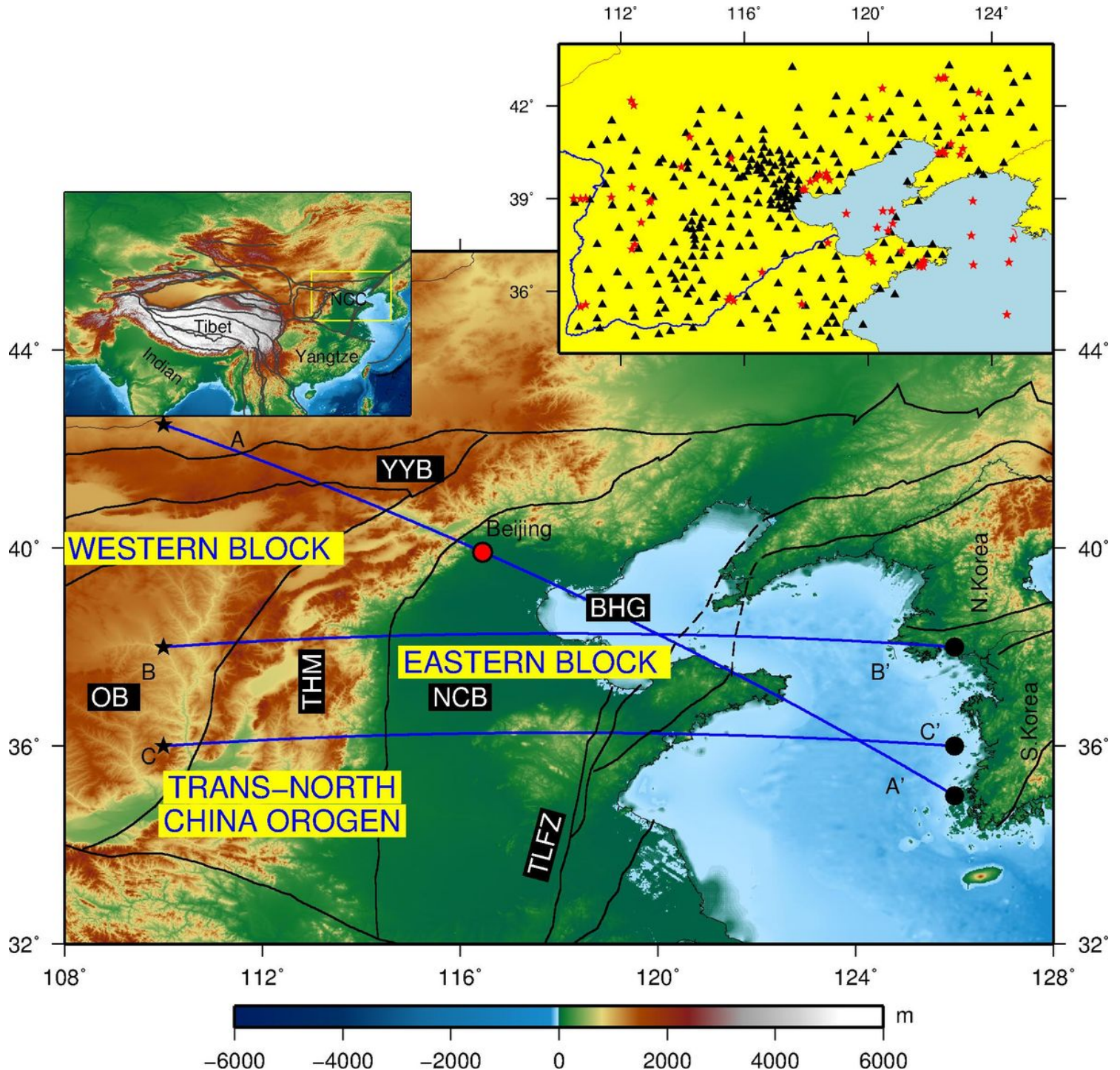


Figure 1

Geological and topographic map of the North China Craton. Blue lines A-A', B-B' and C-C' indicate the location of three vertical profiles. YYB: Yinshan-Yanshan Block; OB: Ordos Block; THM: Taihang Mountains; NCB: North China Basin; BHG: Bohai Gulf; TLFZ: Tan-Lu Fault Zone. The left inset shows the location of NCC in East Asia; the right inset shows the distribution of earthquakes (red stars) and seismic stations (black triangles) in the study. Note: The designations employed and the presentation of the

material on this map do not imply the expression of any opinion whatsoever on the part of Research Square concerning the legal status of any country, territory, city or area or of its authorities, or concerning the delimitation of its frontiers or boundaries. This map has been provided by the authors.

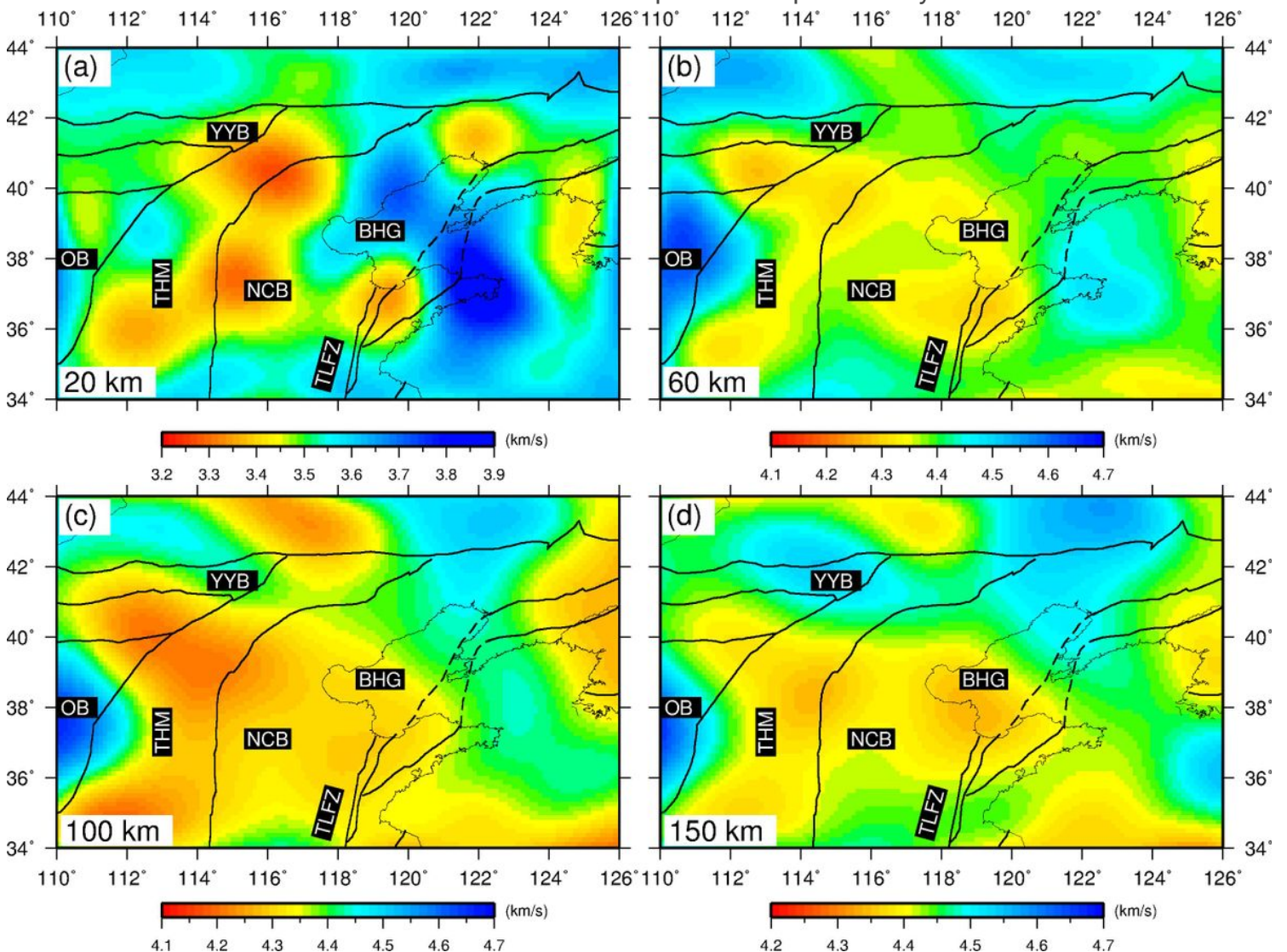


Figure 2

Map views of Sv-wave velocity at four depths. (a) 20 km, (b) 60 km, (c) 100 km and (d) 150 km. Note: The designations employed and the presentation of the material on this map do not imply the expression of any opinion whatsoever on the part of Research Square concerning the legal status of any country, territory, city or area or of its authorities, or concerning the delimitation of its frontiers or boundaries. This map has been provided by the authors.

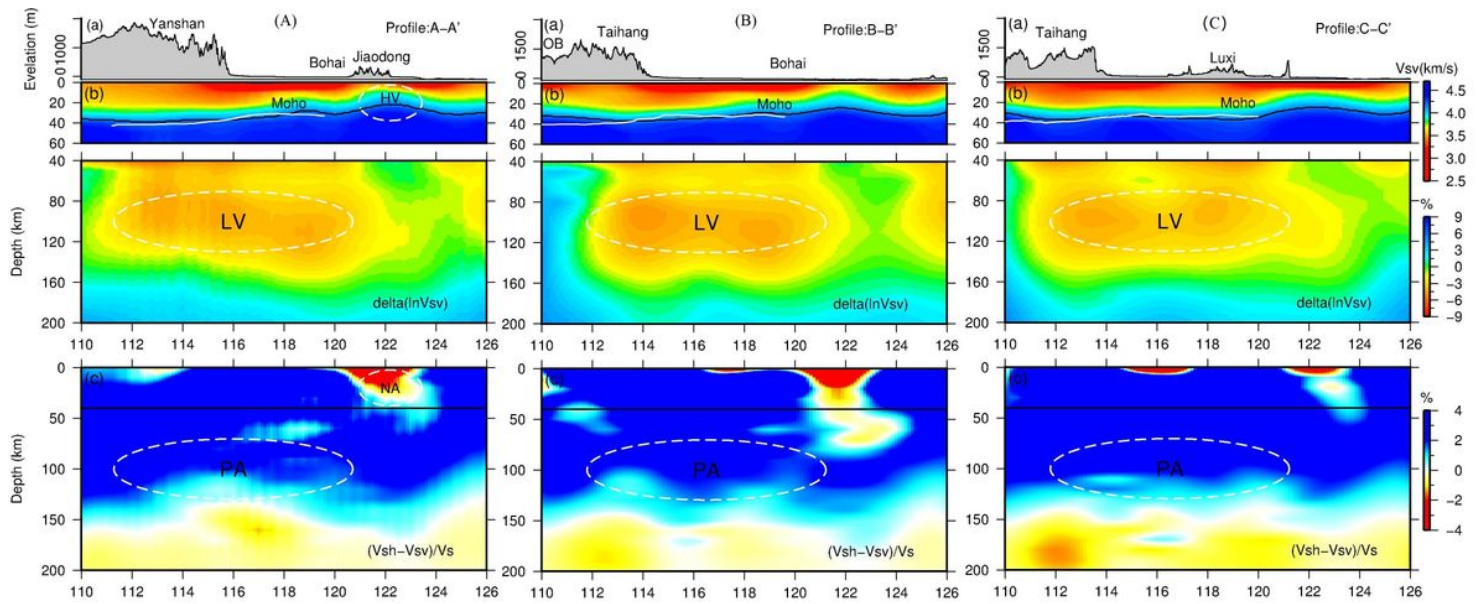


Figure 3

Three vertical cross sections with surface elevation, velocity anomaly and radial anisotropy along profile A-A' (A), B-B' (B) and C-C' (C). Surface altitude (top, a), Sv-wave velocity anomalies (middle, b), and radial anisotropy $(V_{SH}-V_{SV})/V_S$ (bottom, c). For sub-graph b, absolute velocity is adopted for the crust (top 60 km), and velocity perturbation is adopted in upper mantle (40-200 km) with reference model: PREM (Dziewonski & Anderson, 1981). White solid line denotes the depth of Moho obtained from receiver function (Chen 2009; Zheng et al., 2014); black solid line denotes the depth of Moho derived from reference shear wave velocity of 4.2 km/s. LV: low velocity; HV: high velocity; NA: negative anisotropy; PA: positive anisotropy.

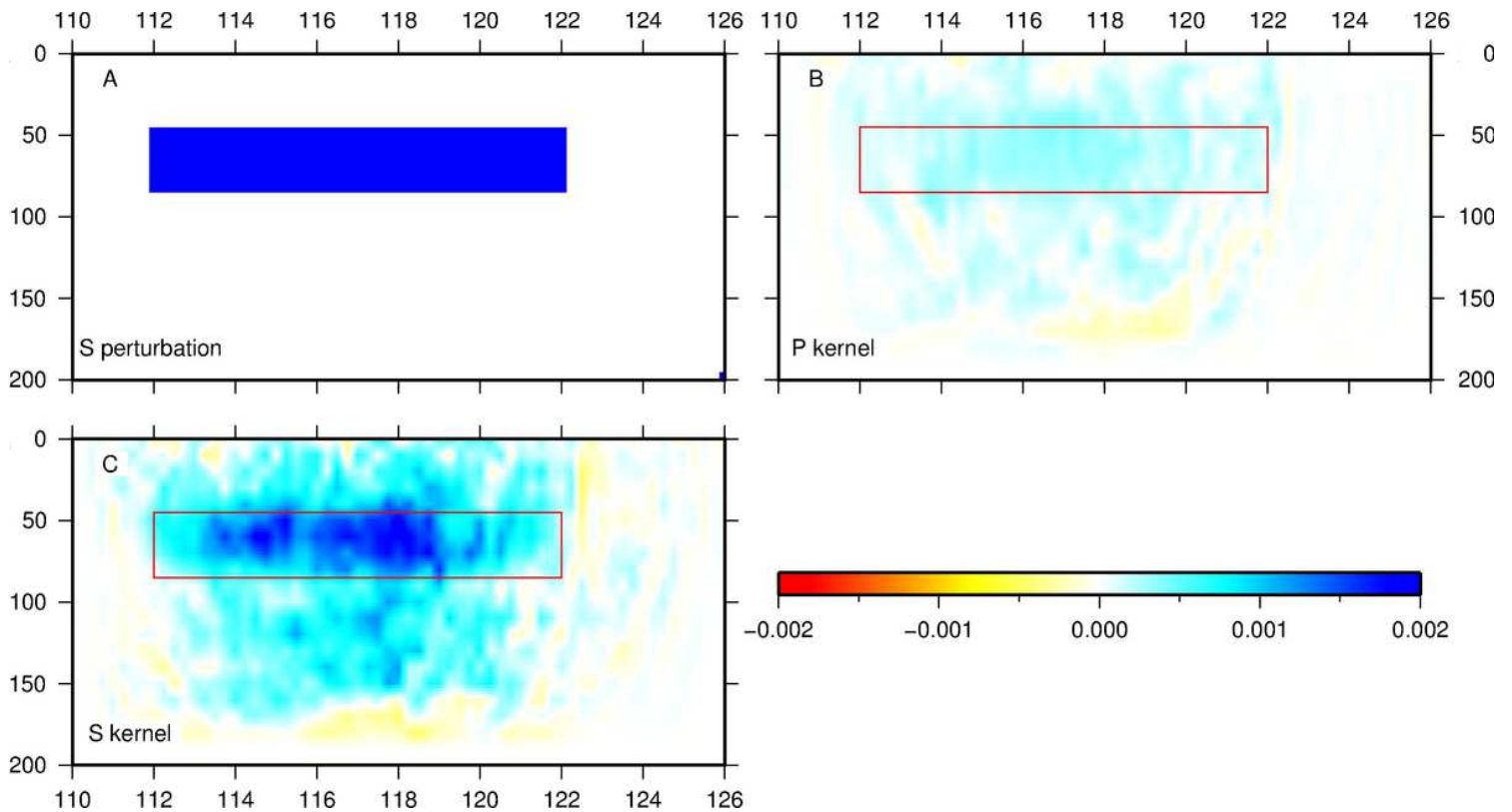


Figure 4

Sensitivity test of Shear wave in the lower crust along 37° N between the depth of 45 km and 85 km. (a) input high Shear velocity perturbation, (b) sensitivity kernel of P wave, (c) sensitivity kernel of S wave. The unit of the color bar is $1 \times 10^{-10} \text{ s}^2 \text{m}^{-4}$.

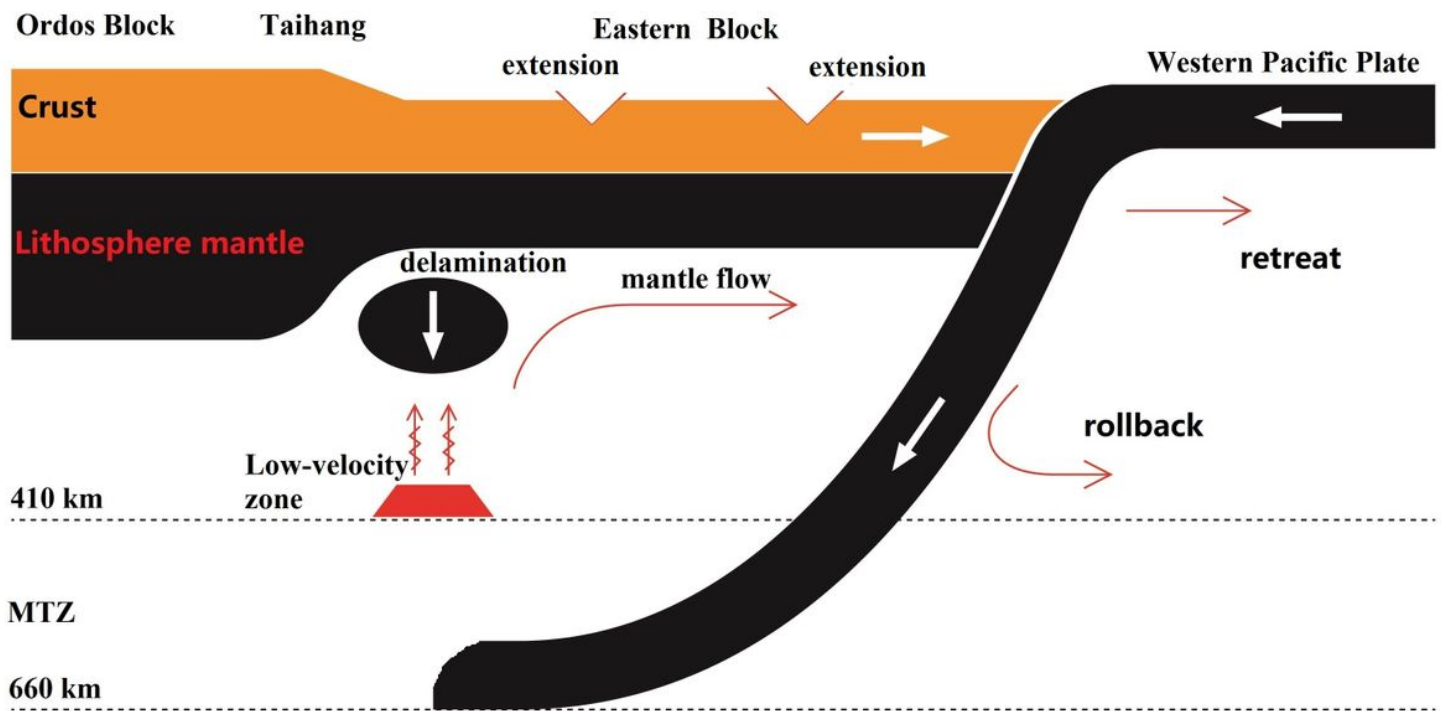


Figure 5

The subduction, rollback and retreat of the western Pacific Plate cause the delamination, horizontal mantle flow and continental crust extension of the NCC. The red trapezoidal area represents the low-velocity zone formed by the subducting slabs squeezing out the water in the mantle transition zone (denotes as MTZ); the water enters the upper mantle and causes partial melting. The black ellipse indicates the delamination of lithosphere due to gravity instability.

Supplementary Files

This is a list of supplementary files associated with this preprint. Click to download.

- [NCCsupport.pdf](#)